Ultrasensitive broadband photodetectors based on two-dimensional Bi_2O_2Te films

Received 00th January 20xx,
Accepted 00th January 20xx

DOI: 10.1039/x0xx00000x

Pin Tian,[a,b] Hongbo Wu,[c] Libin Tang,*[a,b] Jinzhong Xiang,[b,d] Rongbin Ji,[a] Shu Ping Lau,*[e] Kar Seng Teng,*[f] Wei Guo,*[c] Yugui Yao*[c] and Lain-Jong Li[g]

Two-dimensional (2D) materials exhibit many unique optical and electronic properties that are highly desirable for application in optoelectronics. Here, we report the study of photodetector based on 2D Bi_2O_2Te grown on n-Si substrate. The 2D Bi_2O_2Te material was transformed from sputtered Bi_2Te_3 ultrathin film after rapid annealing at 400 ℃ for 10 min in air atmosphere. The photodetector was capable of detecting a broad wavelength ranging from 210 nm to 2.4 µm with excellent responsivity of up to $3x10^5$ and $2x10^4$ AW^{-1}, and detectivity of $4x10^{15}$ and $2x10^{14}$ Jones at deep ultraviolet (UV) and short-wave infrared (SWIR) under weak light illumination, respectively. The effectiveness of 2D materials in weak light detection was investigated by analysis of the photocurrent density contribution. Importantly, the facile growth process using low annealing temperature would allow direct large-scale integration of the 2D Bi_2O_2Te materials with complementary metal-oxide–semiconductor (CMOS) technology.

Introduction

Since the discovery of graphene,[1] there has been enormous interests in 2D materials, either layered[2-6] or non-layered,[7-10] due to their fascinating and unique properties as compared to their bulk counterparts.[10-12] Over the past decade, many 2D materials have found exciting applications in the field of optoelectronics[13-20], such as photocatalyses,[21-23] photodetectors,[24-26] solar cells[27,28] and light-emitting diodes (LEDs).[29-31] Their extraordinary performances in optoelectronics are attributed to its high electron mobility, large specific surface area and energy band tunability. This has led to a significant increase in research activities on 2D materials for application in optoelectronics. Recently, Peng[32] et al. synthesized a 2D Bi_2O_2Se material, which was different from traditional van der Waals 2D layered structure as its layers were held together by relatively weak electrostatic forces.[33-35] Interestingly, the 2D Bi_2O_2Se nanoflakes prepared by chemical vapor deposition (CVD) method exhibited ultrahigh Hall mobility value of >20,000 $cm^2V^{-1}s^{-1}$ and bandgap energy of ~0.8 eV that depended strongly on the film thickness due to quantum-confinement effects. This has led to an increasing research interests in the investigation of 2D bismuth oxychalcogenide

a. Kunming Institute of Physics, Kunming 650223, P.R. China.
b. Yunnan Key Laboratory of Advanced Photoelectric Materials & Devices, Kunming 650223, P.R. China.
c. Beijing Key Laboratory of Nanophotonics and Ultrafine Optoelectronic Systems and Micro-nano Centre, School of Physics, Beijing Institute of Technology, Beijing 100081, China.
d. School of Physics and Astronomy, Yunnan University, Kunming 650091, P.R. China.
e. Department of Applied Physics, The Hong Kong Polytechnic University, Hong Kong SAP, P.R. China.
f. College of Engineering, Swansea University, Bay Campus, Fabian Way, Swansea SA1 8EN, United Kingdom.
g. School of Materials Science and Engineering, University of New South Wales, Sydney 2052, Australia.
† These authors contributed equally.
Electronic Supplementary Information (ESI) available: [details of any supplementary information available should be included here]. See DOI: 10.1039/x0xx00000x

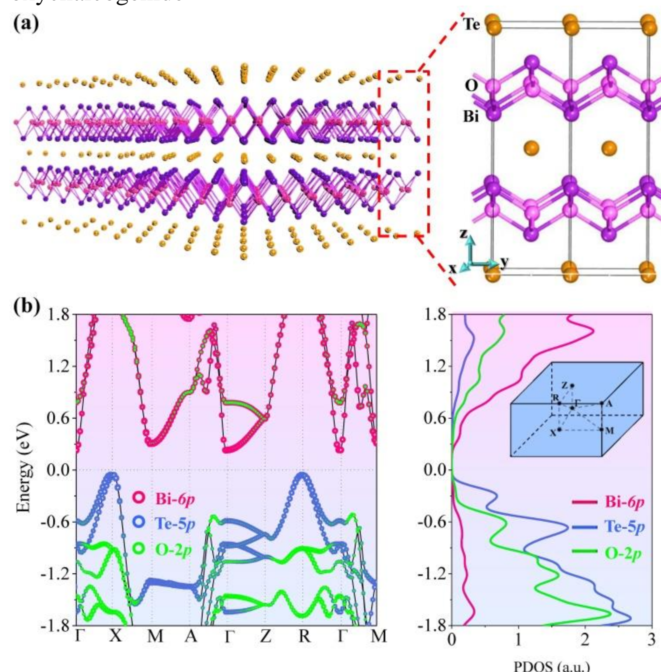

Fig. 1 Crystal structure and band-structure of bulk Bi_2O_2Te. (a) Bulk crystal structure (left) and side view (right) of the layer-dependent atomic structure of Bi_2O_2Te with space group I4/mmm (no. 139). (b) Band-structure (right panel) and the projected partial density of state (PDOS) of Bi2O2Te. Contributions of Bi-*6p*, Te-*5p*, and O-*2p* states are represented by pink, blue, and green circles, respectively. The Brillouin zone is shown as inset in right panel of (b). The Fermi level is shifted to zero.

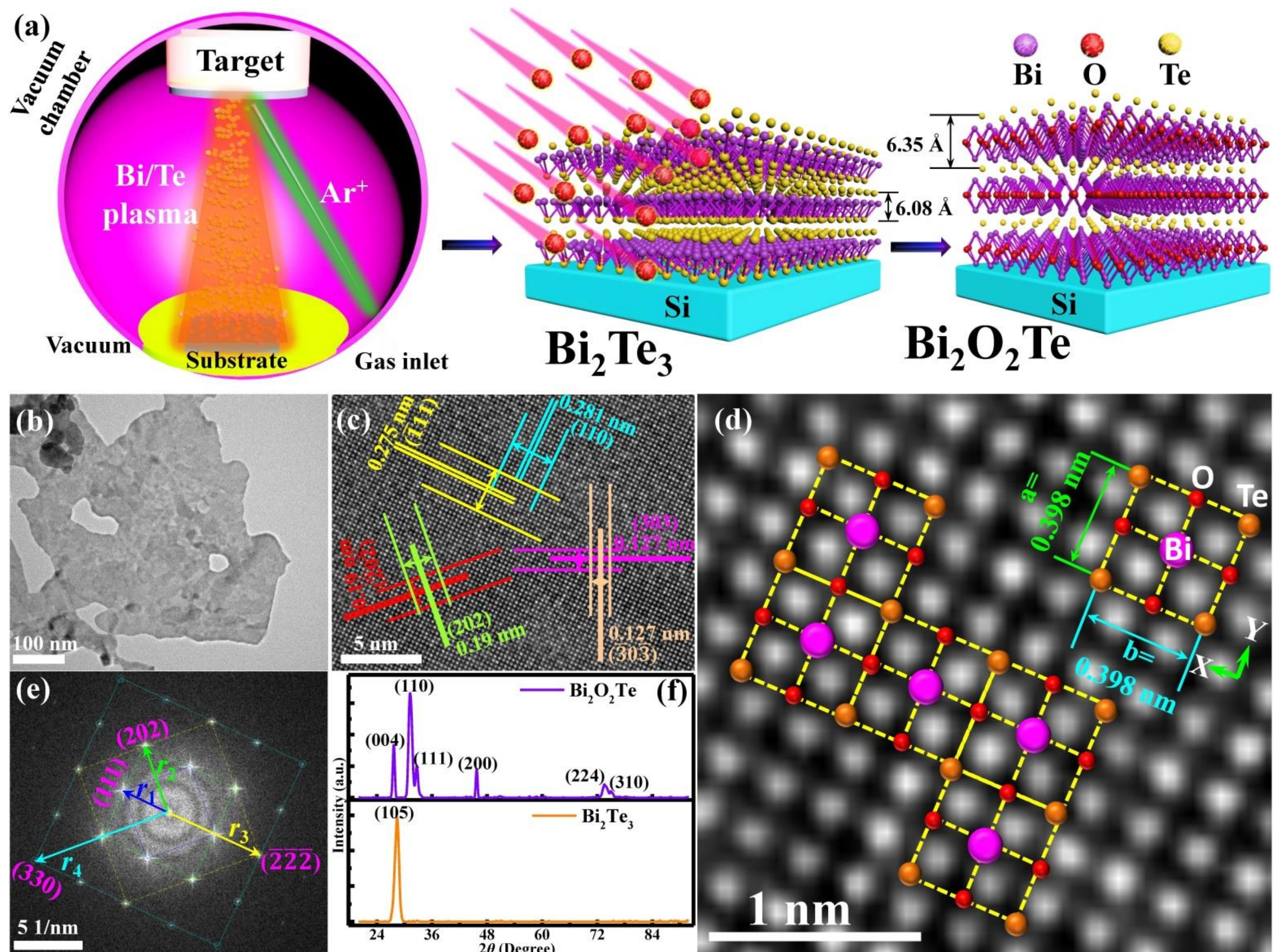

Fig. 2 Growth mechanism and characterization of 2D Bi_2O_2Te prepared by RATP method. (a) Schematic illustration of the structural transformation from the sputtered Bi_2Te_3 to Bi_2O_2Te film by rapid annealing. (b) The TEM image of Bi_2O_2Te. (c) High resolution transmission electron microscopy (HRTM) image of Bi_2O_2Te. (d) HRTEM image of Bi_2O_2Te with grid consisting of different colored dots representing the structure of Bi_2O_2Te (inset shows the crystal structure diagram of Bi_2O_2Te along (001) superimposed on the image). (e) Fast Fourier transform (FFT) image, which indicates diffraction patterns of a square crystal structure. (f) X-ray diffraction (XRD) patterns of Bi_2Te_3 and Bi_2O_2Te.

(Bi_2O_2X: X = S, Se, Te) family. However, 2D Bi_2O_2Te, which is a cousin material of Bi_2O_2Se, was rarely investigated to date. It consists of a tetragonal structure with I4/mmm space group (a = 3.98 Å, c = 12.70 Å) of planar covalently bonded oxide layers (Bi_2O_2) sandwiched by Te square arrays with relatively weak electrostatic interactions (as illustrated in Fig. 1(a)). The preparation of 2D Bi_2O_2Te material by CVD method remains a challenge due to the active characteristics of Te element, thus requires an extensive difference in the evaporation temperatures of Bi precursor and Te source during the growth process.

The different electronegativity[36] of Te (i.e., 2.10) and Se (i.e., 2.55) is very likely to endow Bi_2O_2Te with higher mobility and wider absorption spectrum than Bi_2O_2Se. In addition, the ease of oxidation of Te would allow 2D Bi_2O_2Te material to oxidize at much lower temperature during the preparation of dielectric layer. Such low temperature process is critical to the widespread application of 2D bismuth oxychalcogenide in the field of microelectronics.

While most 2D materials were synthesized using CVD method, the use of magnetron sputtering and rapid thermal annealing to prepare novel 2D Bi_2O_2Te materials at low temperature by transition from Bi_2Te_3 to Bi_2O_2Te under air atmosphere is reported herein. The technique is termed as rapid annealing phase transition (RAPT) method. In this work, a large-area 2D Bi_2O_2Te with excellent quality was prepared by the RAPT

method. There has been much interest in integrating 2D materials with CMOS as demonstrated by Goossens et al..[37] However, the high temperature needed for CVD growth and the difficulty in layer transfer of 2D materials on a wafer scale has hindered the immediate integration of 2D materials with CMOS. Thus, the low temperature growth method (e.g., below tolerable CMOS process temperature of 400℃) can considerably simplify the integration process via direct growth of the 2D materials on CMOS platform. In this work, a photodetector based on the low temperature growth of 2D Bi_2O_2Te was fabricated and characterized. It responded to a broad wavelength range between 210 nm and 2.4 μm with high responsivity of up to $3x10^5$ and $2x10^4$ AW^{-1}, and detectivity of $4x10^{15}$ and $2x10^{14}$ Jones for ultraviolet (UV) and short-wave infrared (SWIR), respectively. The photodetector demonstrated ultra-sensitivity in weak light detection.

The ability of 2D materials in detecting weak light is still not well understood even though various 2D materials based photodetectors had been reported. By analyzing the contribution of photocurrent, the weak light detection capability is possibly attributed to the high separation efficiency of carriers generated in Bi_2O_2Te film. Briefly, this work demonstrates the preparation of Bi_2O_2Te nanofilms by sputtering for the first time. The thickness of the film varied from 4 to 18 nm depending on the ultrashort sputtering duration between 1 and 15 s. This novel 2D material is different from other Van der Waals and non-layered 2D materials, such as graphene, MoS_2, and PbS. Besides, the transition from Bi_2Te_3 to Bi_2O_2Te can be realized simply by rapid annealing at 400 ℃ for 10 min. Such process would enable future integration of Bi_2O_2Te with CMOS technology. Furthermore, the broadband photodetector, consisting of Bi_2O_2Te and n-Si, was fabricated and capable of detecting wavelength between 210 and 2400 nm with ultra-sensitivity. For example, the R (Responsivity) of the photodetector can reach up to 3 x 10^5 and 2 x 10^4 AW^{-1} at deep UV and SWIR, respectively. Also, the D^* (Detectivity) can reach up to 4 x 10^{15} and 2 x 10^{14} Jones for deep UV and SWIR, respectively. The performance of the Bi_2O_2Te/n-Si photodetector is far better than that of current state-of-the-art photodetectors based on Si hybrid 2D materials. The results of this work will have a significant impact in the field of 2D materials as well as ultrasensitive photodetectors.

Results and discussion

Compared to Bi_2O_2Se, the 2D Bi_2O_2Te exhibits a smaller bandgap of ~0.3 eV. Bulk Bi_2O_2Te calculations were performed at fixed experimental lattice constants. Fig. 1(a) shows the layer-dependent atomic structure of tetragonal Bi_2O_2Te verified by DFT calculations. As shown in Fig. 1(b), the calculated band structure indicates that this system is an indirect narrow-gap semiconductor, with the valence band maximum (VBM) at X and the conduction band minimum (CBM) at Γ. From the projected density of states (PDOS), the low-energy electronic states close to Fermi level are primarily contributed by Bi-*6p* and Te-*5p* states with a small fraction of O-*2p* states. The VBM and CBM states are mainly originated from the Te *5p*-orbital and Bi *6p*-orbital bands, respectively. Notably, both CMB and VBM states at Γ and X possess sharp dispersions along Γ-X/Γ-M and X-Γ/X-M directions respectively, hence demonstrating strong in-plane interaction. The MBJ+SOC calculated bandgap (Γ-X) is ~0.28 eV, which is slightly larger than HSE+SOC value of ~0.17 eV, and is in good agreement with the optical bandgap experiments and previous theoretical work.[38,39] Besides, the variation of bandgap with the number of layers has been calculated theoretically (results are shown in Fig. S1-2, ESI†). The bandgap of 2D Bi_2O_2Te film gradually decreases with increasing film thickness, and reaches convergence at ~6 layers (e.g. thickness of ~ 40Å), which is consistent with experimental observations (details in Discussion S4, ESI†). Fig. 2(a) depicts the growth process of 2D Bi_2O_2Te film from sputtered Bi_2Te_3 followed by rapid annealing under air atmosphere (detailed parameters in Methods). TEM characterization of the Bi_2O_2Te film is shown in Fig. 2(b). Fig. 2(c) shows HRTEM image of the film with measurements of lattice spacing along different crystal orientations, which indicate good quality crystal was prepared. The top view crystal structure of Bi_2O_2Te along c-axis (as shown schematically as inset in Fig. 2(d)) can perfectly superimpose on to the magnified HRTEM image from Fig. 2(c). As shown in Fig. 2(d), each white spot could be surrounded with one Bi atom, one Te atom and two O atoms. Besides, Fig. 2(e) shows the FFT image with distinctive diffraction patterns indicating crystallographic directions of (111), (202), ($\overline{222}$) and (330) (details in Discussion S6). HRTEM images on the film, as shown in Fig. S4(a) and (b), ESI†, exhibited crystalline structure with crystal spacing of 0.281 nm along (110). The crystalline phase transition of the as-grown 2D materials was characterized using XRD (Fig. 2(f)). The Bi_2Te_3 has a strong peak at 2θ = 28°, which was along (105). After rapid annealing, it experienced a phase transition to Bi_2O_2Te exhibiting multiple peaks at 2θ = 27.63°, 31.21°, 32.65°, 45.71°, 73.63°, 75.07°, which were along (004), (110), (111), (200), (224) and (310), respectively (details in Table S1). The polycrystalline structure of the 2D Bi_2O_2Te film is shown in Fig. 2(f), which consisted of numerous islands of crystal attributed to the polycrystalline structure of the Bi_2Te_3 precursor (Fig. S5(c-d) and 6(a-d), ESI†). The XRD pattern in Fig. 2(f) is consistent with the TEM and FFT images, which indicate good crystal quality of the Bi_2O_2Te film.

The chemical bond in Bi_2O_2Te was investigated using XPS. The XPS survey spectrum in Fig. 3(a) shows Bi, O and Te elements. The Bi_{4f} core level peak consisted of $Bi_{4f7/2}$ (158.2 eV) and $Bi_{4f5/2}$ (164.1 eV)[40] (Fig. 3(b)). The O_{1s} core level peak was

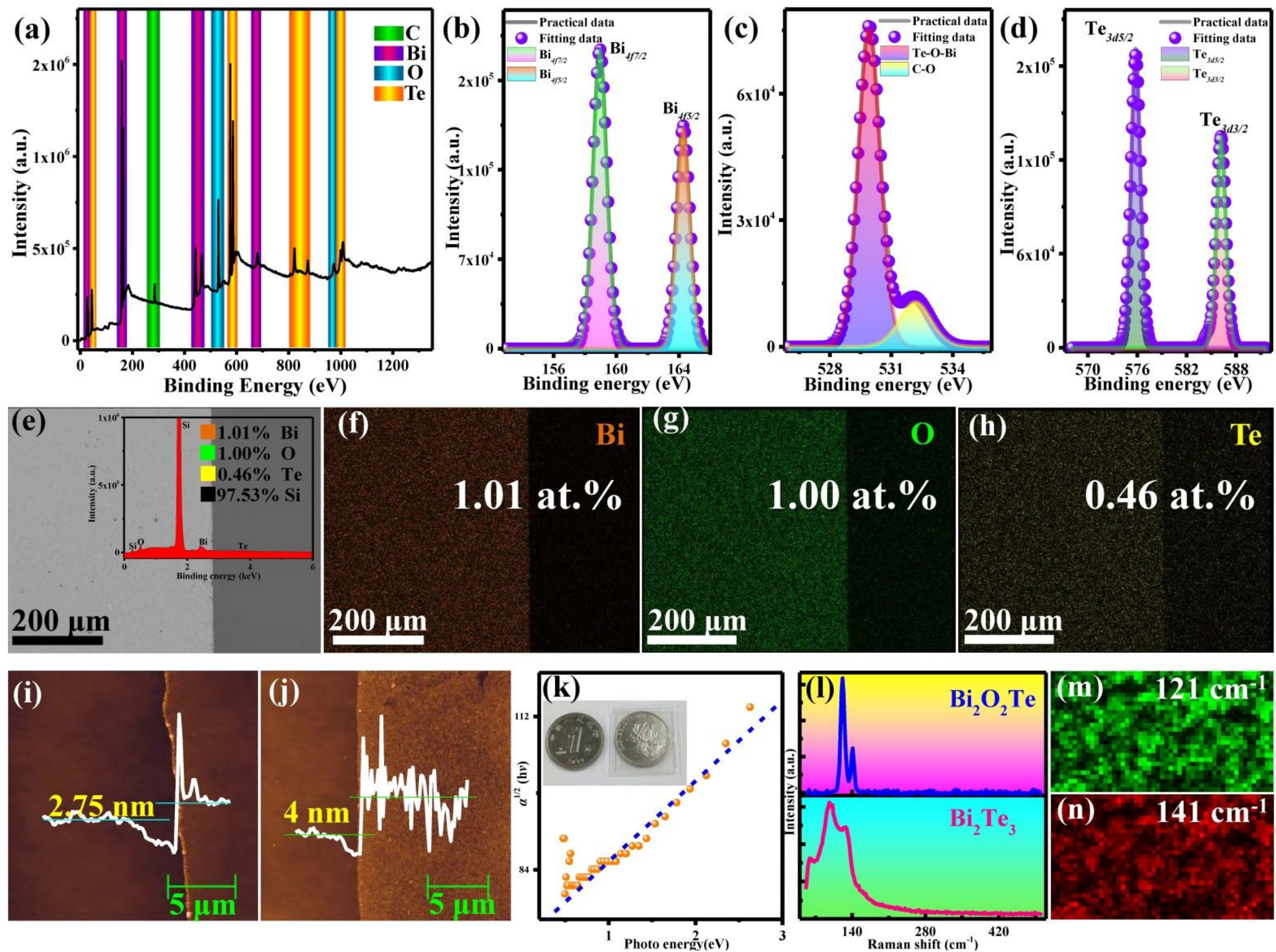

Fig. 3 Structural and morphology characterization of 2D Bi_2O_2Te. (a-d) X-ray photoelectron spectroscopy (XPS) of 2D Bi_2O_2Te showing XPS survey spectrum on the film (a), spectra on core level of Bi_{4f} (b), O_{1s} (c) and Te_{3d} (d). (e) Scanning electron microscopy (SEM) images of Bi_2O_2Te film. (f), (g) and (h) Elemental mapping of Bi, O and Te of 2D Bi_2O_2Te grown on Si substrate, respectively. Inset of (e) shows the ratio of different elements calculated from energy dispersive spectroscopy (EDS) analysis. (i) and (j) Atomic force microscope (AFM) image of Bi_2Te_3 and Bi_2O_2Te film, respectively. (k) Calculated optical bandgap of Bi_2O_2Te. Inset of (k) shows optical images of Bi_2O_2Te contrasted by coin. (l) Raman spectra of Bi_2Te_3 and Bi_2O_2Te. (m) and (n) display the Raman mapping at 121 cm^{-1} and 141 cm^{-1}, respectively.

fitted with two components, namely Te-O-Bi (529 eV) and C-O (532.4 eV)[41,42] (Fig. 3(c)). The core level peak of Te3d was represented by $Te_{3d5/2}$ (575.8 eV) and $Te_{3d3/2}$ (586.2 eV)[43] (Fig. 3(d)). The XPS results indicated that the Bi, O and Te elements were chemically bonded instead of physically mixed. The 2D Bi_2O_2Te film was characterized using TEM to study its crystal structure and morphology. Elemental mapping using EDX was performed on the as-grown Bi_2O_2Te film to determine its stoichiometry as shown in Fig. 3(e-h). The EDS spectrum is shown in Fig. 3(e), and the elemental ratio is also provided in Fig. 3(f-h). The elemental ratio of Bi, O and Te is about 1.01%, 1% and 0.46%, respectively hence indicating that the Bi_2O_2Te has a chemical stoichiometric ratio of 2:2:1. Fig. 3(i) and (j) show the as-grown Bi_2Te_3 and Bi_2O_2Te films having a thickness of 2.75 and 4 nm, respectively as measured using AFM. This suggests that the films consisted of 5-6 layers according to the interlayer distance of Bi_2Te_3 and Bi_2O_2Te crystals (Fig. 2(a)), therefore demonstrating successful formation of the 2D materials. The thickness of the film can be controlled by sputtering duration as shown in Fig. S7(a-f), ESI†. Besides, there was an obvious

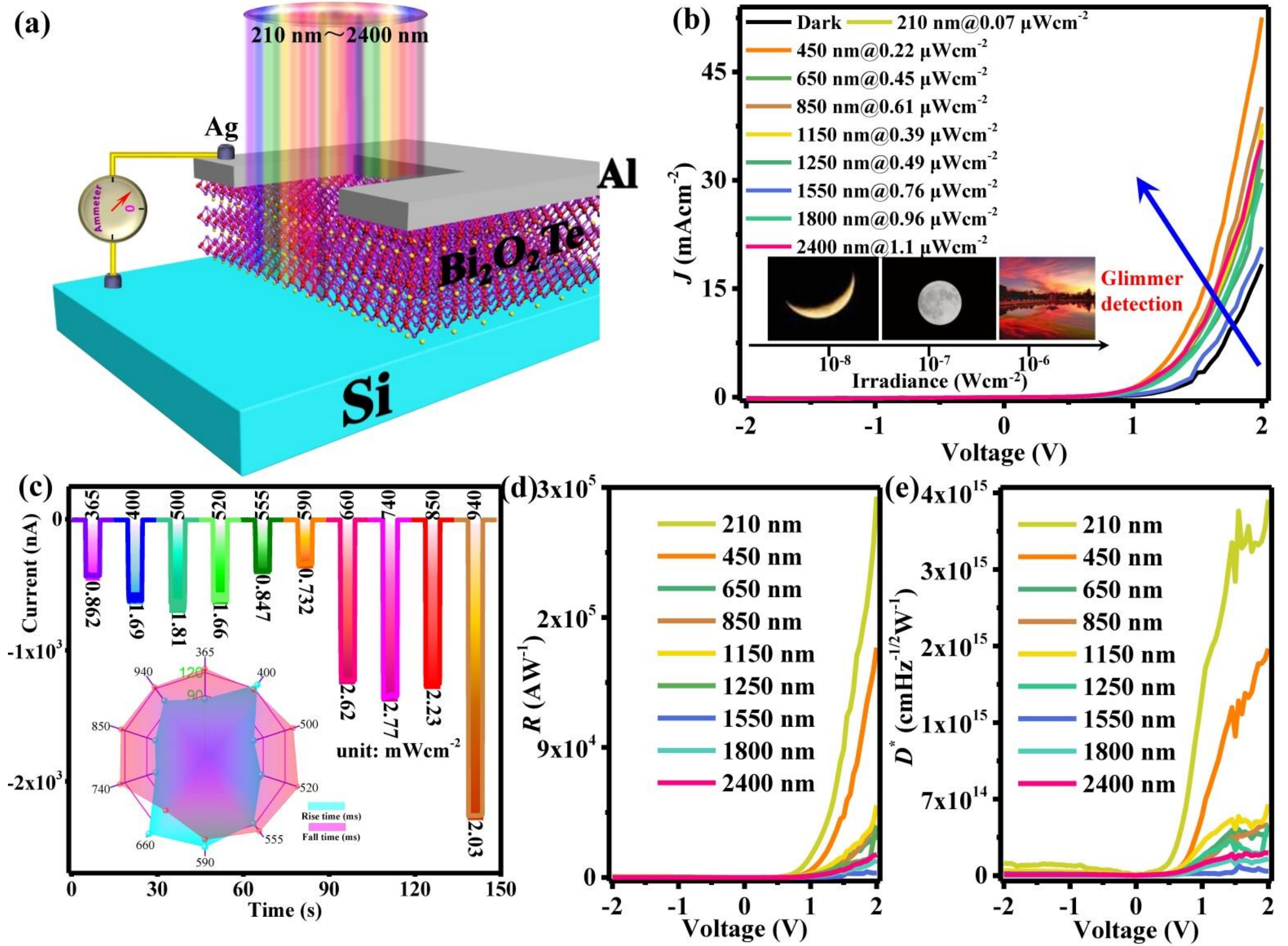

Fig. 4 Characterization of photodetector based on 2D Bi_2O_2Te. (a) Schematic diagram showing the structure of photodetector, composed of 2D Bi_2O_2Te and n-Si substrate, with an active area of 4 mm^2 and responding to a broad wavelength between 210 nm and 2.4 μm. (b) I-V curves of the photodetector in dark and under weak light illumination at different wavelengths. Inset pictures illustrating the variation of light power density for crescent, plenilune and sunset ranging from nanowatt (nW) to microwatt (μW). (c) Transient response of photodetector at -2V applied voltage under LEDs illumination with various wavelengths at milliwatt power density (mWcm^{-2}). The inset diagram depicts the response time, which shows most rise time was shorter than fall time. (d) and (e) Responsivity and detectivity against voltage curves at different wavelengths under weak light illumination with the same power density as (b), respectively.

difference in optical properties between Bi_2Te_3 and Bi_2O_2Te as shown in Fig. S8(a) and Fig. S9(a), ESI†. The Bi_2Te_3 has an optical bandgap of ~0.14 eV (Fig. S9(b), ESI†), which is in good agreement with previously reported works,[40,44-45] while the measured bandgap of Bi_2O_2Te was ~0.3 eV (Fig. 3(k) and details in Discussion S5, ESI†).

SEM image shows uniform coverage of the film on Si substrate and the film exhibited microstructures of 2D Bi_2O_2Te. Moreover, the size of the microstructures in 2D Bi_2O_2Te would increase with sputtering duration of Bi_2Te_3 precursor (details in Fig. S10(a-d), ESI†). The transition from Bi_2Te_3 to Bi_2O_2Te can also be observed on Raman spectra as shown in Fig. 3(l). The classical Raman shift of Bi_2Te_3 is shown in the bottom panel of Fig. 3(l), which revealed four Raman peaks at 62.7, 93.4, 124.1 and 140.3 cm^{-1} corresponding to A^1_{1g}, E^2_g, A_{1u}, and A^2_{1g} of Bi_2Te_3,[46] respectively. As compared to Bi_2Te_3, the Raman spectrum of Bi_2O_2Te (top panel of Fig. 3(l)) shows several new peaks at higher wavenumber, 141 cm^{-1} (A_{1g}),[39] while a different

wavenumber located at 121 cm^{-1} can be observed, which was attributed to the novel 2D structure of Bi_2O_2Te. Furthermore, Raman mapping was performed at 121 and 141 cm^{-1} (as shown in Fig. 3(m) and (n), respectively) indicating uniform film was formed.

A photodetector composed of Al, Bi_2O_2Te and n-Si, as illustrated in Fig. 4(a), was fabricated (details on fabrication process in Experimental). It is worth noting that the Bi_2O_2Te exhibited p-type conductivity (Table S2 provides a list of electronic properties of Bi_2O_2Te, ESI†). The rectification characteristics of the photodetectors with different thickness of Bi_2O_2Te film were investigated to determine the effect of film thickness on the built-in electric field in the device. It was found that the rectification behavior of the photodetector was worsened as the thickness of Bi_2O_2Te film increases (details in Fig. S11(a), ESI†). An optimal performance was observed in the photodetector with a Bi_2O_2Te thickness of 4 nm (e.g., sputtering duration of 1 s). Under weak light illumination, there was an increase in current density of the photodetector, hence indicating the generation of photocurrent as shown in Fig. 4(b) and Fig. S11(b), ESI†. In addition, strong light source from LEDs was incident on the photodetectors, which exhibited similar photovoltaic effect as shown in Fig. S12(a) and (b), ESI†. Transient response of the photodetector was measured under LEDs illumination at a range from 365 to 940 nm. The photodetector displayed stable and fast response with rise and fall time of 77.63 and 126.73 ms at 740 nm, respectively (as shown in Fig. 4(c) and Fig. 13(a-j), ESI†). The rise and fall times under different incident light wavelengths were measured and shown schematically as inset in Fig. 4(c). Figures of merit, such as responsivity and detectivity, are often used to determine and compare the performance of photodetectors. For instance, responsivity can be expressed using the equation:[47]

$$R = J_{ph}/P_{opt} \quad (1)$$

where Jph is photocurrent that equals to the absolute value of the current density under illumination subtracting that in the dark, and Popt is incident optical power. Detectivity (D^*) can be expressed using the equation:[47]

$$D^* = R/\sqrt{2q|J_{dark}|} \quad (2)$$

where J_{dark} is dark current density and q is unit charge. Both R and D^* can be calculated from the I–V characteristic curves. As shown in Fig. 4(d) and (e), the photodetector exhibited excellent performance demonstrating detectable wavelength from 210 nm to 2.4 µm with responsivity of up to 3×10^5 and 2×10^4 AW^{-1}, and detectivity of 4×10^{15} and 2×10^{14} Jones at deep ultraviolet (UV) and short-wave infrared (SWIR) under weak light illumination, respectively. Moreover, the external quantum efficiency (EQE) can reach up to 6000 % as shown in Fig. S18, ESI†. To the best of our knowledge, the performance of the photodetector outperformed those photodetectors based on 2D materials hybrid with Si as depicted in Fig. S15(a-d), ESI†. Previous work reported on photodetector based on PbS quantum dots and graphene showed that a reasonable gain was achieved due to a relatively large difference in the carrier mobility of the two materials.[48,49] Similarly, the observed gain in Bi_2O_2Te/n-Si photodetector could due to a large difference in the mobility of the sputtered 2D Bi_2O_2Te and silicon (e.g., the mobility of the former is far less than that of the latter). Therefore, the holes are trapped in the 2D Bi_2O_2Te while the electrons are transported via silicon, and the excitons generated at the interface between 2D Bi_2O_2Te and silicon are efficiently separated to enhance the performance of the device. The performance of the photodetector under strong light illumination using LEDs was also investigated (as shown in Fig. S12(c) and (d), ESI†). However, the photodetector under strong light illumination exhibited poor performance as compared to weak light illumination. The voltage and current noise spectra of the photodetector were studied and represented in Fig.S16 and Fig. S17(b), respectively, ESI†. Besides, relevant parameters of the photodetector were also calculated and plotted in Fig. S17(d), ESI†. The performance evaluation of the 2D Bi_2O_2Te based photodetector under direct current (DC) as well as alternating current (AC) mode was discussed in Discussion S8, ESI†. Further investigation was carried out to understand the effect of light current density on the performance of the photodetector. The contribution of current density from incident light on the photodetector, which composed of Bi_2O_2Te and Si, was attributed mainly by two parts, such as Bi_2O_2Te side with smaller bandgap energy (E_{g2}) and Si side with wider bandgap energy (E_{g1}) in an ideal case. Given the thickness of device (H) includes thickness of Si (x_1) and Bi_2O_2Te (x_2), as shown in Fig. 5(b), the light current density of the device can be expressed as follow:

$$J_L = \int_0^{\infty}\int_0^{H} qG_L(x)\,dx\,d\lambda \quad (3)$$

where, J_L is light current density, q is unit charge, H is thickness of device, and $G_L(x)$ is rate of generation of photocarriers at position x. The $G_L(x)$ can be expressed using the equation:

$$G_L(x) = N_{ph}(\lambda)\beta[1-R(\lambda)]\alpha(\lambda)e^{-\alpha(\lambda)x} \quad (4)$$

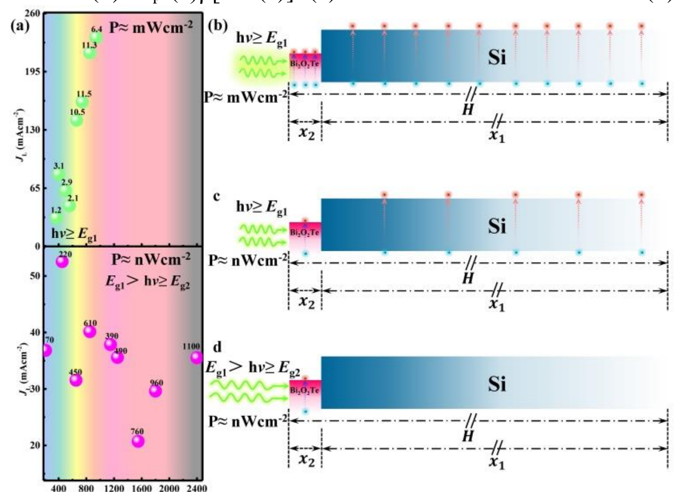

Fig. 5 Light current density contribution analysis. (a) The light current density (J_L) spectrum of photodetector with applied voltage of 2 V under illumination of strong light source at milliwatt level (top) and weak light source at nanowatt level (bottom). (b-d) Photoelectric transport mechanism under different power irradiation of light sources with different wavelengths. (b) Strong light with energy h$\nu \geqslant E_{g1}$ (bandgap of Si) incident on the device and both sides (Bi_2O_2Te and Si) generate abundant excitons. (c) Weak light with energy h$\nu \geqslant E_{g1}$, both sides generate excitons but the number of electron-holes pair is less than that of strong light due to a decrease in the number of photons. (d) Weak light with $E_{g1} >$ h$\nu \geqslant E_{g2}$, only one side with smaller bandgap (e.g. E_{g2}, bandgap of Bi_2O_2Te) can generate excitons due to a decrease in photons energy.

where $N_{ph}(\lambda)$ is number of photons with specific wavelength (λ) incident on device, β is probability of a photon producing a pair

Please do not adjust margins

of photocarriers (e.g., β=1 if photon energy (hν) is larger than bandgap of semiconductor, otherwise β=0), $R(\lambda)$ is surface reflectance relative to wavelength, $\alpha(\lambda)$ is absorption coefficient of corresponding wavelength, and x is position of photocarriers. Since the photodetector was composed of different materials, which have different $R(\lambda)$, $\alpha(\lambda)$ and bandgap, the $G_L(x)$ can be divided into two parts, namely $G_L(x)_{Si}$ on the Si side and $G_L(x)_{Bi2O2Te}$ on the Bi_2O_2Te side, which can be expressed as:

$$G_L(x)= G_L(x)_{Si} + G_L(x)_{Bi2O2Te} \quad (5)$$

As the thickness of Si (400μm) was much larger than that of Bi_2O_2Te (4 nm), the $G_L(x)$ is therefore dominated by $G_L(x)_{Si}$ if the photon energy h$\nu \geq E_{g1}$ (Si bandgap). As shown in Fig. 5(b) and (c), both Bi_2O_2Te and Si sides would generate excitons but the number of excitons under weak light would be less than that of strong light due to a reduction in the photon number $N_{ph}(\lambda)$ of weak light. This inner mechanism is revealed in the light current density as shown in Fig. 5(a). In the case of wavelength less than 1100 nm, which is the detection limit of Si, the light current density of weak light is distinctively smaller than that of strong light. However, in the case of $E_{g1}>$ h$\nu \geq E_{g2}$, the β of Si is zero, so $G_L(x)_{Si}=0$ and $G_L(x)=G_L(x)_{Bi2O2Te}$. Considering the saturation absorption characteristic of 2D materials due to the dominance of surface state,[50] the strong light illuminated on 2D Bi_2O_2Te would be ineffective as the ultrathin 2D materials do not fully convert all incoming photons into electron-hole pairs. As shown in the bottom panel of Fig. 5(a), the light current density of weak light illumination ($E_{g1}>$ h$\nu \geq E_{g2}$) is of the same order as strong light (h$\nu \geq E_{g1}$) but the performance of the photodetector under weak light is much better than that of strong light (see Fig. 4(c) and (d), and Fig. S12(c) and (d), ESI†). Therefore, the 2D materials is more capable of detecting weak light, instead of strong light, than the bulk materials due to its surface state saturation absorption characteristics.

Conclusion and future aspects

In this work, we have successfully developed a novel 2D Bi_2O_2Te material with narrow bandgap prepared by a two-steps method, involving magnetron sputtering and rapid annealing. The 2D material was investigated by systematic theoretical calculations and multiple characterization techniques to confirm the transition of Bi_2Te_3 to Bi_2O_2Te by rapid annealing under air atmosphere at 400 ℃. An ultrasensitive photodetector consisting of 2D Bi_2O_2Te and n-Si heterojunction was fabricated for weak light detection. The Bi_2O_2Te nanofilm was prepared by sputtering of Bi_2Te_3 for 1 s and then followed by rapid annealing at 400 ℃ for 10 min in air atmosphere. The photodetector was capable of detecting a broad wavelength of light ranging from 210 nm to 2400 nm with responsivity of up to $3x10^5$ and $2x10^4$ AW^{-1}, and detectivity of $4x10^{15}$ and $2x10^{14}$ Jones at deep UV and SWIR under weak light illumination, respectively. Due to surface state saturation absorption characteristics of the 2D material, the device exhibited much better performance under weak light illumination than strong light. In summary, we have reported the growth of a novel 2D Bi_2O_2Te material using the sputtering method, which is suitable for large-scale chip integration with CMOS technology. This 2D material has shown excellent performance as weak light photodetector with many potential applications. The 2D Bi_2O_2Te material has potential applications in the detection of mid-wave infrared. It can also be used to improve the performance of silicon based solar cells through enhancing the absorption of weak light or infrared spectrum. Furthermore, since the 2D Bi_2O_2Te material has played vital roles as hole transport layer (HTL) and absorption layer in enhancing the performances of the photodetector, this novel 2D materials can also be used as HTL or active layer in various infrared detectors, such as colloidal quantum dots photodetectors.

Experimental

Theoretical section

Structural optimization and band-structure calculations were performed based on density functional theory (DFT) as implemented in the Vienna ab-initio simulation package (VASP).[51,52] The projector-augmented-wave (PAW) method was utilized to describe the interactions between the ionic cores and the valence electrons.[53,54] The Bi $6s^26p^3$, Te $5s^25p^4$ and O $2s^22p^4$ orbitals were explicitly included as valence electrons. The general gradient approximation of Perdew-Burke-Ernzerhof (PBE-GGA) was employed to treat the electronic exchange-correlation effects.[55] Electronic wave functions were expanded using a plane wave basis set with an energy cutoff of 500 eV. The ionic relaxations were performed until the force on each atom was less than 0.01 $eVÅ^{-1}$ and convergence criterion for the self-consistent electronic minimization loop was set to 10^{-5} eV. The Brillouin zone was sampled using a Monkhorst-Pack scheme during structure relaxations.[56] Due to the well-known underestimation of bandgap of PBE-GGA functional for semiconductors, the general gradient approximation-modified Becke-Johnson (GGA-MBJ)[57] method was adopted to compute the bandgap of bulk Bi_2O_2Te with spin orbit coupling (SOC) effect included.

The 2D thin film of Bi_2O_2Te structure was computed using a slab model. To keep the inversion symmetry of the bulk phase, both the top and bottom layers were terminated with Te atoms. To balance the non-stoichiometry due to the additional Te layers, hydrogen atoms were chosen to passivate the outermost Te layers. Similar structural treatment was adopted by Wu et al.[32] In vacuum, the electron density and kinetic energy density of MBJ method are close to zero, thus the MBJ calculations tend to diverse for 2D systems. To achieve high calculation accuracy, the hybrid Heyd-Scuseria-Ernzerhof (HSE) functional[58] was adopted for calculating the bandgap of Bi_2O_2Te thin film. The HSE06+SOC bandgap calculations were too computationally expansive for large systems, thus we performed HSE06 bandgap calculations with SOC correction from differences between GGA+SOC vs GGA results. The thickness of vacuum layer was set to 15 Å to avoid periodic interactions. The van der Waals interaction was taken into account with the DFT-D3 method.[59]

Preparation of 2D Bi_2O_2Te and photodetector

A custom made magnetron sputtering technique (SPS-T-S100N-2G, Weinaworld) was used. Firstly, n-Si substrate, which has a resistivity of 1-10 Ω·cm and crystal orientation along <100>, was cleaned by acetone and ethanol. Next, the substrate was placed

Please do not adjust margins

Please do not adjust margins

in a vacuum chamber (of <4.5x10^{-4} Pa) and annealed at 200℃ in Ar (60sccm) for 10 min with working pressure kept at 5 Pa. The Bi_2Te_3 target (99.99%, purchased from ZhongNuoXinCai) was sputtered by radio frequency (RF) at 200 W for 1, 5, 10 and 15 s. Finally, the sputtered Bi_2Te_3 thin films were rapid annealed using RTP-1300 (ECOPiA) for 10 min at 400 ℃ with a rise time of 60 s under air atmosphere. After annealing, the films were left to cool down to room temperature. A uniform Bi_2O_2Te thin film was prepared on Si substrate. Photodetector was fabricated by depositing patterned Al film on the 2D Bi_2O_2Te thin film using a vacuum evaporation technique at pressure less than 6.9x10^{-4} Pa.

Characterization of Bi_2O_2Te and Bi_2Te_3 film

Both Bi_2Te_3 and Bi_2O_2Te thin films were characterized using Raman spectroscopy (XperRam Compact), XRD (EMPYREAN) UV-visible (U-4100) and TEM (Tecnai G2 TF30) techniques. The preparation process of Bi_2O_2Te film for TEM measurement is as follows: firstly, a Si substrate was thinned to a few tens of micron using HF and sputtered with Bi_2Te_3, and then oxidized to form Bi_2O_2Te. Next, the prepared sample was thinned further to remove the Si substrate using an ion milling equipment (691, Gantan). The Bi_2Te_3 film was etched from substrate through HF etching. Elementary composition of the samples was studied using XPS (K-Alpha$^+$) with monochromated Al Kα radiation. Uniformity and thickness of the film was measured using atomic force microscopy (AFM) (Seiko SPA-400) and field-emission scanning electron microscope (SEM, Quanta 200). The Fourier transform-infrared (FTIR) spectra of the Bi_2Te_3 film were acquired by Thermo Nicolet Avatar 360 spectrometer using attenuated total reflection (ATR). Hall measurement was carried out using Hall characterization system (HL5550 LN2 CRYOSTAT).

Characterization of photodetectors

J-V measurements on the photodetector were performed using Keithley 2400 source meter. Strong light source was from LEDs with a variety of wavelengths (e.g. 365, 400, 500, 555, 660, 740 and 850 nm). Weak light source was obtained from deuterium lamp and bromine tungsten lamp (DSR-LSH-D30T75, Zolix) through spectrometer. The transient response measurement was performed using Keithley 2400 source meter with the LEDs driven by function/arbitrary waveform generator (RIGOL, DG 1022U). Besides, the power density of specific wavelength was measured by bolometer (FZ400, NBeT Group Corp) and the power density spectra of the weak light was obtained by spectral responsivity measurement system (DSR100-D30T75) (see Fig. S14, ESI†). The spectra of voltage noise power density of the photodetector based on 2D Bi_2O_2Te was carried out at 0 V by using a lock-in amplifier (HF2LI). All measurements were carried out at room temperature.

Author Contributions

Pin Tian performed the growth of 2D Bi_2O_2Te and prepared the photodetector. Hongbo Wu carried out the theoretical calculation. Libin Tang, Shu Ping Lau, Kar Seng Teng, Wei Guo and Yugui Yao conceived the project. Libin Tang supervised this work. All authors participated in the discussion and contributed to the manuscript.

Conflicts of interest

There are no conflicts to declare.

Acknowledgements

This work was supported by National Key Research and Development Program (Grant No. 2019YFB2203404), National Natural Science Foundation of China (Grant No. 61106098, 51201150, 11374250 and 11864044), the Key Project of Applied Basic Research of Yunnan Province, China (Grant No. 2012FA003), and the Hong Kong Polytechnic University grant (1-ZVGH).

Notes and references

1 K. S. Novoselov, A. K. Geim, S. V. Morozov, D. Jiang, Y. Zhang, S. V. Dubonos, I. V. Grigorieva and A. A. Firsov, *Science* 2004, **306**, 666-669.
2 M. C. Watts, L. Picco, F. S. Russell-Pavier, P. L. Cullen, T. S. Miller, S. P. Bartuś, O. D. Payton, N. T. Skipper, V. Tileli and C. A. Howard, *Nature* 2019, **568**, 216-220.
3 J. Yang, Z. Zeng, J. Kang , S. Betzler, C. Czarnik, X. Zhang, C. Ophus, C. Yu, K. Bustillo, M. Pan, J. Qiu, L.-W. Wang and H. Zheng , *Nat. Mater.* 2019, **18**, 970-976.
4 Z. Fei, B. Huang, P. Malinowski, W. Wang, T. Song, J. Sanchez, W. Yao, D. Xiao, X. Zhu, A. F. May, W. Wu , D. H. Cobden, J.-H. Chu and X. Xu , *Nat. Mater.* 2018, **17**, 778-782.
5 C. H. Lui, L. Liu, K. F. Mak, G. W. Flynn and T. F. Heinz, *Nature* 2009, **462**, 339-341.
6 I. V. Vlassiouk, Y. Stehle, P. R. Pudasaini, R. R. Unocic, P. D. Rack, A. P. Baddorf , I. N. Ivanov , N. V. Lavrik, F. List, N. Gupta, K. V. Bets, B. I. Yakobson and S. N. Smirnov, *Nat. Mater.* 2018, **17**, 318-322.
7 F. Wang, J.-H. Seo, G. Luo, M. B. Starr, Z. Li, D. Geng, X. Yin, S. Wang, D. G. Fraser, D. Morgan, Z. Ma and X. Wang, *Nat. Commun.* 2016, **7**, 10444.
8 F. Wang, Z. Wang, L. Yin, R. Cheng, J. Wang, Y. Wen, T. A. Shifa, F. Wang, Y. Zhang, X. Zhana and J. He, *Chem. Soc. Rev.* 2018, **47**, 6296-6341.
9 S. Liu, L. Xie, H. Qian, G. Liu, H. Zhong and H. Zeng, *J. Mater. Chem. A* 2019, **7**, 15411-15419.
10 C. Zhu, D. Gao, J. Ding, D. Chao and J. Wang, *Chem. Soc. Rev.* 2018, **47**, 4332-4356.
11 N. Mounet , M. Gibertini , P. Schwaller, D. Campi, A. Merkys , A. Marrazzo , T. Sohier , I. E. Castelli, A. Cepellotti, G. Pizzi and N. Marzari, *Nat. Nanotechnol.* 2018, **13**, 246-252.
12 J. Zhou, J. Lin, X. Huang, Y. Zhou, Y. Chen, J. Xia, H. Wang, Y. Xie, H. Yu, J. Lei, D. Wu, F. Liu, Q. Fu, Q. Zeng, C.-H. Hsu, C. Yang, L. Lu, T. Yu, Z. Shen, H. Lin, B. I. Yakobson, Q. Liu, K. Suenaga, G. Liu and Z. Liu , *Nature* 2018, **556**, 355-359.
13 S. Aftab, Samiya, H. M. Ul Haq, S. Yousuf, M. U. Khan, Z. Ahmed, J. Aziz, M. W. Iqbal, A. ur Rehman and M. Z. Iqbal, *Adv. Mater. Interfaces* 2020, **7**, 2001479.
14 S. Aftab, I. Akhtar, Y. Seo and J. Eom, *ACS Appl. Mater. Interfaces* 2020, **12**, 42007-42015.
15 S. Aftab, M. F. Khan, P. Gautam, H. Noh and J. Eom, *Nanoscale* 2019, **11**, 9518-9525
16 S. Aftab, Samiya, M. W. Iqbal, P. A. Shinde, A. ur Rehman, S. Yousuf, S. Park and S. C. Jun, *Nanoscale* 2020, **12**, 18171-18179.
17 S. Aftab, Samiya, Rabia, S. Yousuf, M. U. Khan, R. Khawar, A. Younus, M. Manzoor, M. W. Iqbal and M. Z. Iqbal, *Nanoscale* 2020, **12**, 15687-15696.

This journal is © The Royal Society of Chemistry 20xx

Please do not adjust margins

Please do not adjust margins

18 S. Aftab, M. Samiya, H. M. Ul Haq, M. W. Iqbal, M. Hussain, S. Yousuf, A. Ur Rehman, M. U. Khan, Z. Ahmed and M. Z. Iqbal, *J. Mater. Chem. C* 2021, **9**, 199-207.
19 S. Aftab, M. Samiya, Ali Raza, M. W. Iqbal, H. M. Ul Haque, K. Ramachandraiah, S. Yousuf, S. C. Jun, A. Ur Rehman and M. Z. Iqbal, *Nanotechnology* 2021, **32**, 285701.
20 S. Aftab, M. F. Khan, K.-A. Min, G. Nazir, A. M. Afzal, G. Dastgeer, I. Akhtar, Y. Seo, S. Hong and J. Eom, *Nanotechnology* 2018, **29**, 045201.
21 C. Tan, X. Cao, X.-J. Wu, Q. He, J. Yang, X. Zhang, J. Chen, W. Zhao, S. Han, G.-H. Nam, M. Sindoro and H. Zhang , *Chem. Rev.* 2017, **117**, 6225-6331.
22 A. Dhakshinamoorthy, A. M. Asiri and H. Garcia, *Adv. Mater.* 2019, 1900617.
23 X. Zhu, T. Zhang, D. Jiang, H. Duan, Z. Sun, M. Zhang, H. Jin, R. Guan, Y. Liu, M. Chen, H. Ji, P. Du, W. Yan, S. Wei, Y. Lu and S. Yang, *Nat. Commun.* 2018, **9**, 4177.
24 H. Lin , Y. Song, Y. Huang, D. Kita, S. Deckoff-Jones, K. Wang, L. Li, J. Li, H. Zheng, Z. Luo, H. Wang, S. Novak, A. Yadav, C.-C. Huang, R.-J. Shiue, D. Englund, T. Gu, D. Hewak, K. Richardson, J. Kong and J. Hu, *Nat. Photon.* 2017, **12**, 798-805.
25 M. Long, A. Gao, P. Wang, H. Xia, C. Ott, C. Pan, Y. Fu, E. Liu, X. Chen, W. Lu, T. Nilges, J. Xu, X. Wang, W. Hu and F. Miao, *Sci. Adv.* 2017, **3**, e1700589.
26 K. F. Mak and J. Shan, *Nat. Photon.* 2016, **10**, 216-226.
27 T. Kato, M. Yoshio, T. Ichikawa, B. Soberats, H. Ohno and M. Funahashi, *Nat. Rev.* 2017, **2**, 17001.
28 D. Jariwala, T. J. Marks and M. C. Hersam, *Nat. Mater.* 2016, **16**, 170-181.
29 F. Withers, O. Del Pozo-Zamudio, A. Mishchenko, A. P. Rooney, A. Gholinia, K. Watanabe, T. Taniguchi, S. J. Haigh, A. K. Geim, A. I. Tartakovskii and K. S. Novoselov , *Nat. Mater.* 2015, **14**, 301-306.
30 H. Tsai, W. Nie, J.-C. Blancon, C. C. Stoumpos, C. M. M. Soe, J. Yoo, J. Crochet, S. Tretiak, J. Even, A. Sadhanala, G. Azzellino, R. Brenes, P. M. Ajayan, V. Bulović, S. D. Stranks, R. H. Friend, M. G. Kanatzidis and A. D. Mohite, *Adv. Mater.* 2018, **30**, 1704217.
31 M. C. Weidman, A. J. Goodman and W. A. Tisdale, *Chem. Mater.* 2017, **29**, 5019-5030.
32 J. Wu, H. Yuan, M. Meng, C. Chen, Y. Sun, Z. Chen, W. Dang, C. Tan, Y. Liu, J. Yin, Y. Zhou, S. Huang, H. Q. Xu, Y. Cui, H. Y. Hwang, Z. Liu, Y. Chen, B. Yan and H. Peng, *Nat. Nanotechnol.* 2017, **12**, 530-534.
33 Q. Fu, C. Zhu, X. Zhao, X. Wang, A. Chaturvedi, C. Zhu, X. Wang, Q. Zeng, J. Zhou, F. Liu, B. K. Tay, H. Zhang, S. J. Pennycook and Z. Liu, *Adv. Mater.* 2019, **31**, 1804945.
34 P. Luo, F. Zhuge, F. Wang, L. Lian, K. Liu, J. Zhang and T. Zhai, *ACS Nano* 2019, **13**, 9028-9037.
35 Y. Liang, Y. Chen, Y. Sun, S. Xu, J. Wu, C. Tan, X. Xu, H. Yuan, L. Yang, Y. Chen, P. Gao, J. Guo and H. Peng, *Adv. Mater.* 2019, 1901964.
36 J. Xiao, Y. Wang, X. Feng, D. Legut, T. Wang,Y. Fan, T. Su, R. Gong, R. Zhang and Q. Zhang, arXiv:1911.11327.
37 S. Goossens, G. Navickaite, C. Monasterio, S. Gupta, J. J. Piqueras, R. Pérez, G. Burwell, I. Nikitskiy, T. Lasanta, T. Galán, E. Puma, A. Centeno, A. Pesquera, A. Zurutuza, G. Konstantatos and F. Koppens, *Nat. Photon.* 2017, **11**, 366-371.
38 M. Wu and X. C. Zeng, *Nano Lett.* 2017, **17**, 6309-6314.
39 T. Cheng, C. Tan, S. Zhang, T. Tu, H. Peng and Z. Liu, *J. Phys. Chem. C* 2018, **122**, 19970-19980.
40 J. G. Checkelsky, J. Ye, Y. Onose, Y. Iwasa and Y. Tokura, *Appl. Phys. Lett.* 2017, **110**, 141109.
41 L. V. Yashina, J. Sánchez-Barriga, M. R. Scholz, A. A. Volykhov, A. P. Sirotina, V. S. Neudachina, M. E. Tamm, A. Varykhalov, D. Marchenko, G. Springholz, G. Bauer, A. Knop-Gericke and O. Rader, *ACS Nano* 2013, **7**, 5181-5191.
42 H. Bando, K. Koizumi, Y. Oikawa, K. Daikohara, V. A. Kulbachinskii and H. Ozaki, *J. Phys.: Condens. Matter.* 2000, **12**, 5607–5616.
43 J. Fu, S. Song, X. Zhang, F. Cao, L. Zhou, X. Lia and H. Zhang, *Cryst. Eng. Comm.* 2012, **14**, 2159.
44 J. G. Checkelsky, J. Ye, Y. Onose, Y. Iwasa and Y. Tokura, *Nat. Phys.* 2012, **8**, 729-733.
45 X. Mu, H. Zhou, D. He, W. Zhao, P. Wei, W. Zhu, X. Niea, H. Liu and Q. Zhang, *Nano Energy* 2017, **33**, 55-64.
46 N. Hussain, Q. Zhang, J. Lang, R. Zhang, M. Muhammad, K. Huang, T. C. De Villenoisy, H. Ya, A. Karim and H. Wu, *Adv. Opt. Mater.* 2018, **6**, 1701322.
47 X. Gong, M. Tong, Y. Xia, W. Cai, J. S. Moon, Y. Cao, G. Yu, C.-L. Shieh, B. Nilsson and A. J. Heeger, *Science* 2009, **325**, 1665-1667.
48 Z. Sun , Z. Liu , J. Li , G.-A. Tai , S.-P. Lau and F. Yan, *Adv. Mater.* 2012, **24**, 5878–5883.
49 R. Saran and R. J. Curry, *Nat. Photon.* 2016, **10**, 81-92.
50 J.-L. Xu, Y.-J. Sun, J.-L. He, Y. Wang, Z.-J. Zhu, Z.-Y. You, J.-F. Li, M. M. C. Chou, C.-K. Lee and C.-Y. Tu, *Sci. Rep*. 2015, **5**, 14856.
51 G. Kresse and J. Furthmüller, *Comput. Mater. Sci.* 1996, **6**, 15-50.
52 G. Kresse and J. Furthmüller, *Phys. Rev. B* 1996, **54**, 11169.
53 P. E. Blöchl, *Phys. Rev. B* 1994, **50**, 17953.
54 G. Kresse and D. Joubert, *Phys. Rev. B* 1999, **59**, 1758.
55 J. P. Perdew, K. Burke and M. Ernzerhof, *Phys. Rev. Lett.* 1996, **77**, 3865.
56 H. J. Monkhorst and J. D. Pack, *Phys. Rev. B* 1976, **13**, 5188.
57 F. Tran and P. Blaha, *Phys. Rev. Lett.* 2009, **102**, 226401.
58 J. Heyd, G. E. Scuseria and M. Ernzerhof, *J. Chem. Phys.* 2003, **118**, 8207-8215.
59 S. Grimme, J. Antony, S. Ehrlich and H. Krieg, *J. Chem. Phys.* 2010, **132**, 154104.

This journal is © The Royal Society of Chemistry 20xx

Please do not adjust margins